Available online at www.sciencedirect.com
SCIENCE DIRECT®
PERGAMON
Vacuum 69 (2003) 545–555
VACUUM
SURFACE ENGINEERING, SURFACE INSTRUMENTATION & VACUUM TECHNOLOGY
www.elsevier.com/locate/vacuum

Characteristics of n-$Cd_{0.9}$ $Zn_{0.1}S$/p-CdTe heterojunctions

M.A. Redwan[a], E.H. Aly[a], L.I. Soliman[b], A.A. El-Shazely[a], H.A. Zayed[a,*]

[a] *University College for Art, Science and Education, Ain Shams University, Cairo, Egypt*
[b] *National Research Center, Cairo, Egypt*

Received 02 August 2002; received in revised form 14 October 2002; accepted 16 October 2002

Abstract

CdTe thin films were prepared by thermal evaporation under a vacuum of 10^{-6} Torr and with a deposition rate of about 60 nm/min. X-ray diffraction studies of the as-deposited films revealed polycrystalline films with cubic structure. The effect of heat treatment with or without $CdCl_2$ enhances the grain size and improves the crystallinity of the films. Moreover, the activation energy decreases upon heat treatment with or without $CdCl_2$ for CdTe thin films. The optical spectra of CdTe films show interference oscillations indicating the good optical quality of these films. The calculated energy gap decreases with or without $CdCl_2$ treatments. The current–voltage and capacitance–voltage characteristics for dark and illuminated three junction cells are measured. By analysing these measurements the different junction parameters are obtained and the effect of $CdCl_2$ treatment on the performance of the heterojunctions is investigated.

Keywords: Semiconductors; Thin films; Solar cells; Optical/electrical properties

1. Introduction

Heterojunction solar cells promise to play a revolutionary role in photovoltaic as an alternative source for future energy needs. Walf [1] was the first who suggested the use of a heterojunction cell with the surface layer of a wide band-gap material as one of the possibilities of improving conversion efficiency. To date many systems of heterojunction solar cells such as p-Cu_2 S/n-CdS, n-CdS/p-CdTe, n-IP/p-Cu_2Se, p-Al_xGa_{1-x} As/n-GaAs, n-CdS/p-$CuInSe_2$ and n-CdS/p-$CuInGaSe_2$ have been investigated [2–9]. Moreover, a considerable activity in research and development has been focused on newer device technologies and newer materials such as quaternaries, pen-ternaries, and graded multi-component semiconductors [10,11]. For instance, CdTe is one of the important materials for the fabrication of high efficiency heterojunction solar cells.

The aim of the present work is to study the physical properties of CdTe thin films and to investigate n-$Cd_{0.9}Zn_{0.1}S$/p-CdTe solar cell heterojunctions.

2. Experimental

2.1. Preparation of CdTe thin films

CdTe thin films were prepared by the conventional thermal evaporation technique using a

*Corresponding author.
E-mail address: sdeeb@main.scc.cairo.eun.eg (H.A. Zayed).

0042-207X/03/$ - see front matter
PII: S0042-207X(02)00604-8

Leybold-Heraeus high vacuum coating unit Univex-300 provided with INFIONXTC thin film thickness and rate controller. The deposition rate and film thickness were controlled with the quartz crystal thickness monitor, deposition rate was 60 nm/min and the film thickness was 2000 nm. CdTe thin films were deposited at substrate temperature $T_s = 473$ K.

2.2. Heterojunctions preparation

The $Cd_{0.9}Zn_{0.1}S$/CdTe cells were prepared in superstrate configuration, so that light enters the cell through a grid over the glass superstrate. First, about 200 nm of $Cd_{0.9}Zn_{0.1}S$ were deposited at 423 K by evaporation onto grid coated glass substrates. Prior to CdTe deposition some of the prepared $Cd_{0.9}Zn_{0.1}S$ films [12], were heat treated with $CdCl_2$ vapour to reduce optical absorption and to minimize diffusion of Te into $Cd_{0.9}Zn_{0.1}S$ during subsequent processing [13]. On the top of the $Cd_{0.9}Zn_{0.1}S$ layer, Cd Te with a thickness of about 2000 nm was then evaporated at a growth rate of about 60 nm/min and a substrate temperature of 473 K. To examine the effect of post deposition treatments, some films were heat treated with $CdCl_2$ vapour [12]. The crystallization of CdTe films at about 673 K was examined through a detailed analysis of the films with or without $CdCl_2$ treatment.

2.3. Structural characterization

The X-ray diffraction (XRD) patterns of CdTe samples in both powder and thin films deposited on glass substrates were recorded by a Philips PW 1373 X-ray diffractometer.

2.4. Optical measurements

The transmittance $T(\lambda)$ and reflectance $R(\lambda)$ of the as-deposited and treated films were measured at normal incidence in the spectral range of 300–2500 nm, using the JASCO model V-570 UV–VIS–NIR double beam spectrophotometer.

2.5. Electrical measurements

Electrical resistivity measurements of the prepared thin films were performed by the coplanar four probe technique in the temperature range from 300 to 500 K using a Keithley 616 digital electrometer. The Hall effect measurements were carried out by the traditional DC method for Hall voltage. The dark current–voltage (I–V) characteristics were carried out at different temperatures, while the illuminated I–V characteristics were performed at room temperature under 85-mW/cm^2 incident light power. The dark capacitance–voltage (C–V) characteristics for the $Cd_{0.9}Zn_{0.1}S$/CdTe heterojunctions were measured at room temperature using a FLUKE programmable automatic RCL meter model PM 6306. Measurements were performed at different frequencies with reverse DC bias voltage scanned from 0 to 2 V at steps of 100 mV.

3. Results and discussion

3.1. Cadmium telluride films

3.1.1. Structural properties

Fig. 1 shows the XRD patterns for the as-deposited CdTe films and those heat-treated with and without $CdCl_2$ at 673 K for 20 min. The lattice parameters calculated from the XRD data are in good agreement with the given value in the standard card (JCPDS). The structure is cubic with a lattice parameter $a = 6.48$ Å which is approximately constant regardless of annealing or $CdCl_2$ heat treatment. The data obtained show that the grain size is increased for films treated with $CdCl_2$ as has been observed for the $CdCl_2$ methanol method [8,14]. Moreover, no extraneous peaks are observed in the XRD pattern.

3.1.2. Electrical properties

The temperature dependence of the electrical conductivity (σ) is given by

$$\sigma = \sigma_0 \exp(-\Delta E/KT),$$

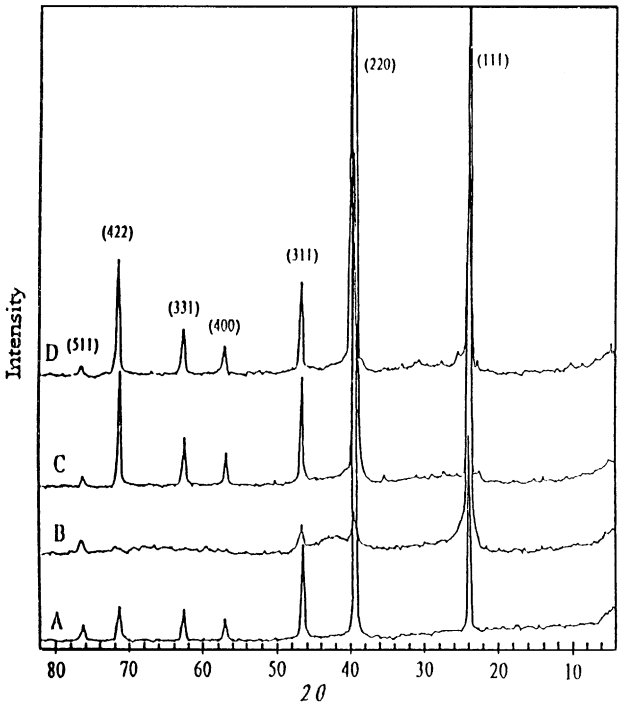

Fig. 1. XRD patterns for CdTe powder (A) and thin films, as deposited (B), annealed for 20 min at 673 K (C) and $CdCl_2$ treated at 673 K for 20 min (D).

where σ_0 is the pre-exponential factor, ΔE is the activation energy, K is Boltzmann's constant and T is the absolute temperature.

The dark electrical conductivity σ of CdTe films with different treatments was measured as a function of the sample temperature in the range from 300 to 473 K. Fig. 2 shows the plot of ln versus $1000/T$ for CdTe films, both as deposited and annealed at 673 K for 20 min with and without $CdCl_2$. Each graph can be divided into two distinct linear parts, which indicates the existence of two activation energies for the conduction free charge carriers, ΔE_1 at temperatures below 373 ± 10 K and ΔE_2 at temperatures above 373 ± 10 K. It is clear from Fig. 2 that neither annealing nor $CdCl_2$ treatment affect the behavior or the value of σ in the high temperature region with the activation energy $\Delta E_2 = 0.711$ eV. However, in the low temperature region, the calculated activation energies ΔE_1 decreased by annealing or $CdCl_2$ treatment, while the room temperature conductivity increased. The decrease in ΔE_1 from 0.409 to

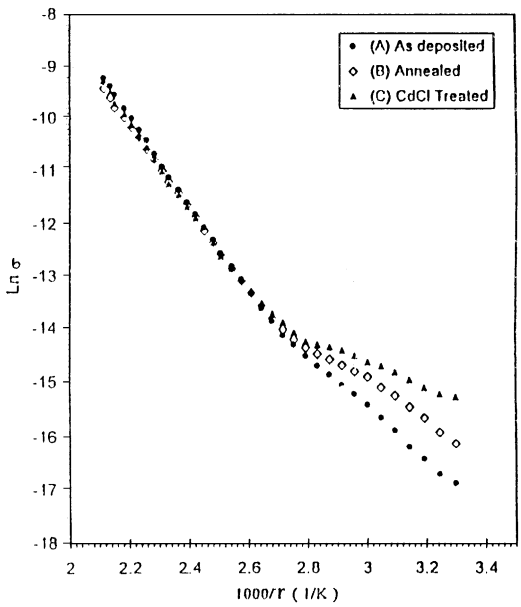

Fig. 2. Temperature dependence of d.c. conductivity σ for CdTe films, as deposited (A), annealed for 20 min at 673 K (B) and $CdCl_2$ treated at 673 K for 20 min (C).

0.01 eV may be attributed to the improvement of the film crystallinity and the larger grain size as indicated by XRD measurements.

3.1.3. Optical properties

The optical constants of the as-deposited CdTe films and those heat treated with or without $CdCl_2$, are obtained from the transmittance $T(\lambda)$ and reflectance $R(\lambda)$ recorded at room temperature. The value of the absorption coefficient α at different wavelengths is calculated using the following relation:

$$T = (1 - R)^2 \exp(-\alpha t)/1 - R^2 \exp(-2\alpha t), \qquad (2)$$

where t is the thickness of the films.

The results are analysed using the relation $\alpha(h\nu) = A(h\nu - E_g)^{1/2}$ for direct transition. Fig. 3 represents the plots of $(\alpha h\nu)^2$ versus photon energy ($h\nu$). The calculated values of the optical energy gap E_g for the as-deposited CdTe films and those heat treated with and without $CdCl_2$ are 1.52, 1.5 and 1.49 eV, respectively. The decrease of the optical energy gap values upon annealing or $CdCl_2$ treatment may be due to the improvement of the film crystallinity [15]. Also the thickness of the films was determined from the interference region of the transmittance $T(\lambda)$. The calculated thickness values compare well with thickness values indicated by the quartz crystal monitor.

3.2. Characterization of $Cd_{0.9}Zn_{0.1}S$/CdTe heterojunctions

One of the major difficulties in the development of n-CdS/p-CdTe heterojunctions is that pin holing occasionally occurs in the CdS film leading to electrical shunting in the final cell. To avoid such a problem $Cd_{0.9}Zn_{0.1}S$ can be used as an alternative window layer for the fabrication of n-$Cd_{0.9}Zn_{0.1}S$/p-CdTe heterojunctions.

In the present work, three different heterojunctions were prepared for examining the consequences of $Cd_{0.9}Zn_{0.1}S$ window layer and the effect of $CdCl_2$ treatment on the properties of the heterojunctions. The prepared cells were fabricated under the same conditions and have the following structure

Cell 1: glass/Au grid/n-CdS/*p*-CdTe/Al

Cell 2: glass/Au grid/n-$Cd_{0.9}Zn_{0.1}S$/p-CdTe/Al

Cell 3: glass/Au grid/n-$Cd_{0.9}Zn_{0.1}S$/p-CdTe/Al, where $Cd_{0.9}Zn_{0.1}S$ is treated with $CdCl_2$ prior to CdTe deposition.

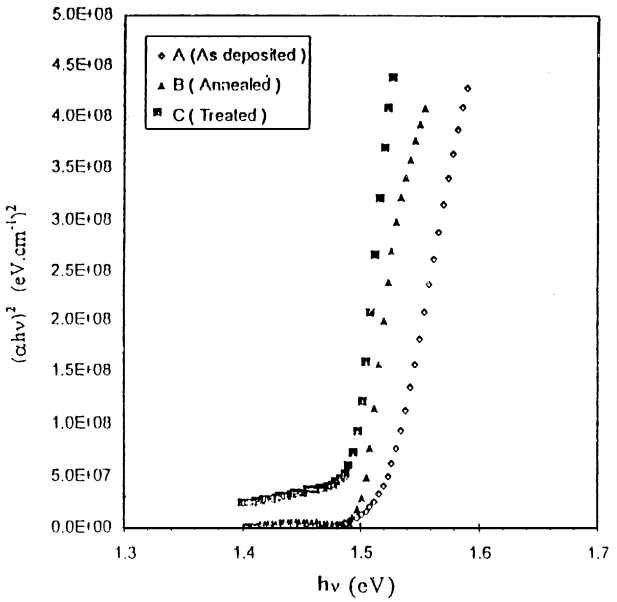

Fig. 3. $(\alpha h\nu)^2$ versus $h\nu$ for CdTe gilms, as deposited (A) annealed for 20 min at 673 K (B) and $CdCl_2$ treated at 673 K for 20 min (C).

3.2.1. I–V characteristics

3.2.1.1. Dark I–V characteristics. *I–V* characteristics as a function of the junction temperature provide a valuable source of information about the junction properties. The dark *I–V* characteristics for the three cells at different temperatures are shown in Figs. 4–6. The forward current shows an exponential increase with the applied voltage. However, at high forward bias ($V > 0.8$ V) the *I–V* characteristics show a linear behaviour. This behaviour indicates a clear effect of the junction series resistance (R_s).

The rectification ratio (RR) for the cells can be calculated from the ratio of the forward current to the reverse current at a certain value of the applied voltage. The calculated values are listed in Table 1. It is obvious that cell 3 has the best rectification, indicating the good performance of this cell.

The value of the series resistance R_s for the cells can be determined from the slope of the linear part of the forward *I–V* characteristics at high bias. Similarly, the shunt resistance (R_p) can be found from the reverse *I–V* characteristics. Moreover, the

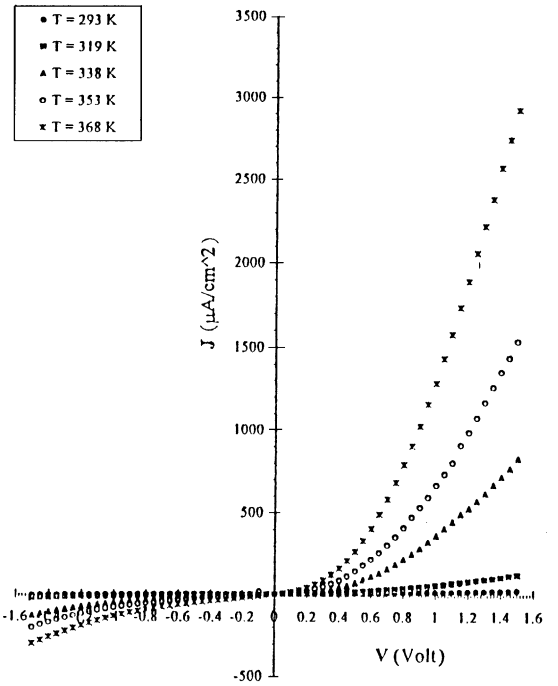

Fig. 5. *I–V* characteristics for Cell 2 at different temperatures.

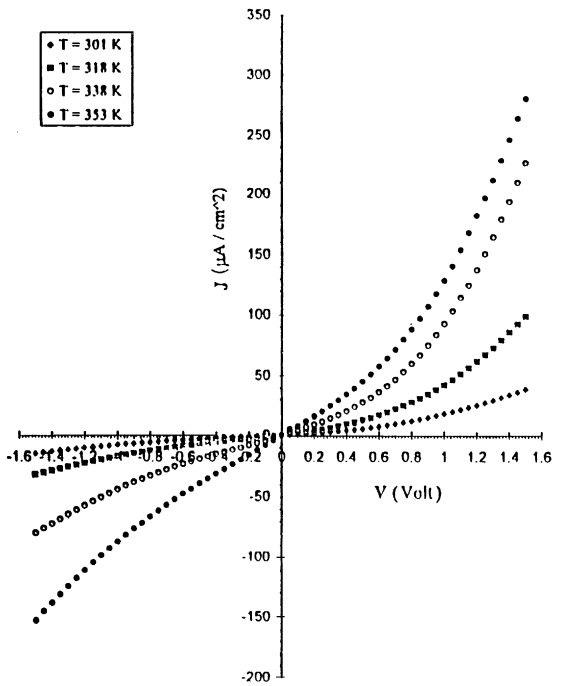

Fig. 4. *I–V* characteristics for Cell 1 at different temperatures.

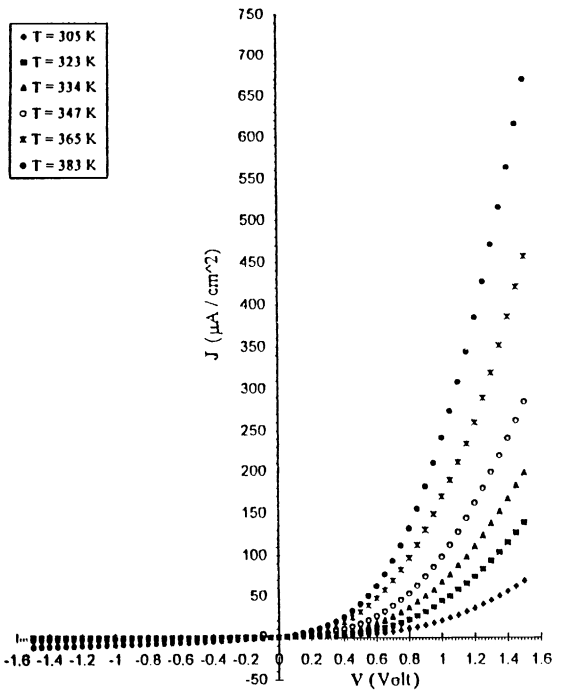

Fig. 6. *I–V* characteristics for Cell 3 at different temperatures.

Table 1
Values of the rectification ratio, the series resistance, the shunt resistance, and the built-in voltage for the threee cells at $T = 300\,\mathrm{K}$

Junction	RR	R_s (kΩ)	R_p (MΩ)	V_D (V)
Cell 1	3	23.5		0.65
Cell 2	10	23.1		0.62
Cell 3	160	11.1		0.80

Table 2
Average values of the forward-current and reverse-current activation energies for the three cells

Junction	ΔE_f (eV)	ΔE_r (eV)
Cell 1	0.35	0.42
Cell 2	0.58	0.46
Cell 3	0.34	0.46

extrapolation of the linear parts of the forward I–V characteristics to the zero current axes may give the value of the built-in voltages. The obtained values of V_D are presented in Table 1. Cell 3 shows the lowest series resistance compared to the other cells, while both cell 1 and cell 2 exhibit a considerable shunting as indicated by the low shunt resistance at high current in the reverse direction. So, cell 3 shows the best performance.

Assuming that the current (forward or reverse) for a given voltage obeys the relation

$$J = \exp(-\Delta E/KT), \tag{3}$$

where J is the current and ΔE is the activation energy, the forward current activation energy (ΔE_f) and the reverse current activation energy (ΔE_r) can be determined by plotting $\ln J$ versus $1000/T$ in the forward and reverse directions, respectively. The obtained average values of ΔE_f and ΔE_r for the three cells are given in Table 2.

The current mechanism present was explored from semi-logarithmic plots of the forward dark I–V characteristics at different temperatures. $\mathrm{Ln}\,J$ versus V plots at different temperatures (300–380 K) for the three cells are shown in Figs. 7–9. The three cells show the same exponential forward characteristics. At low voltage ($V < 0.3\,\mathrm{V}$), the curve can be divided into two distinct linear regions.

In the first region ($V < 0.3\,\mathrm{V}$), the diode quality factor m and the saturation current density J_0 can be evaluated by fitting the experimental data to the diode equation

$$J = J_0 \exp(EV/mKT), \tag{4}$$

where J_0 is given by

$$J_0 = J_{00} \exp(-\Delta E_a/KT) \tag{5}$$

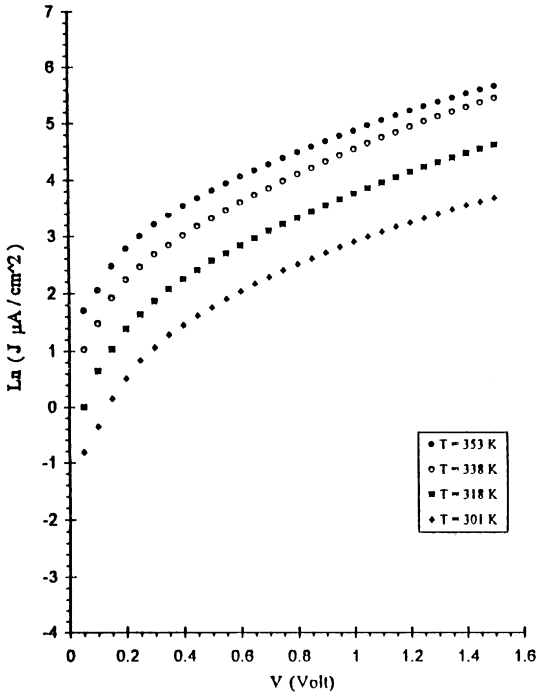

Fig. 7. $\mathrm{Ln}\,J$ versus forward applied bias Cell 1 at different temperatures.

with ΔE_a is being the saturation current activation energy, K the Boltzmann's constant and e the electronic charge. The experimental data are fitted well with Eqs. (4) and (5), which indicate that the current transport is dominated by recombination at the interface. The obtained parameters for the three cells are summarized in Tables 3 and 4. Cell 2 has saturation current density and diode quality factor values lower than those of cell1, while cell 3 exhibits the lowest saturation current and diode quality factor values. The decrease in both the saturation current and the quality factor

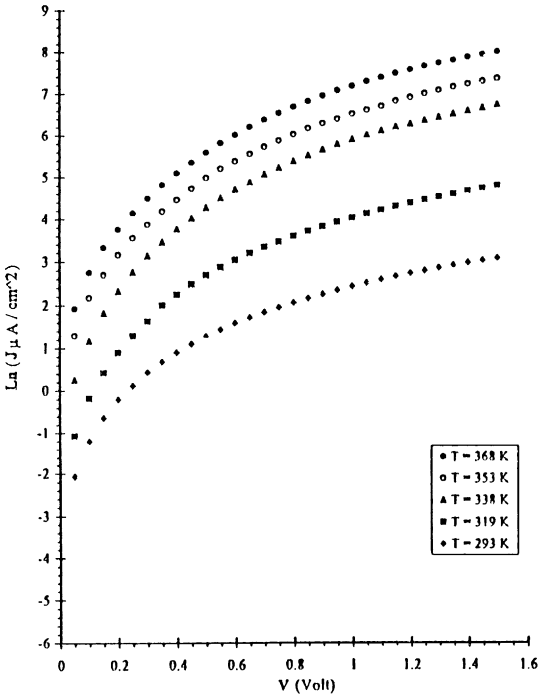

Fig. 8. Ln J versus forward applied bias Cell 2 at different temperatures.

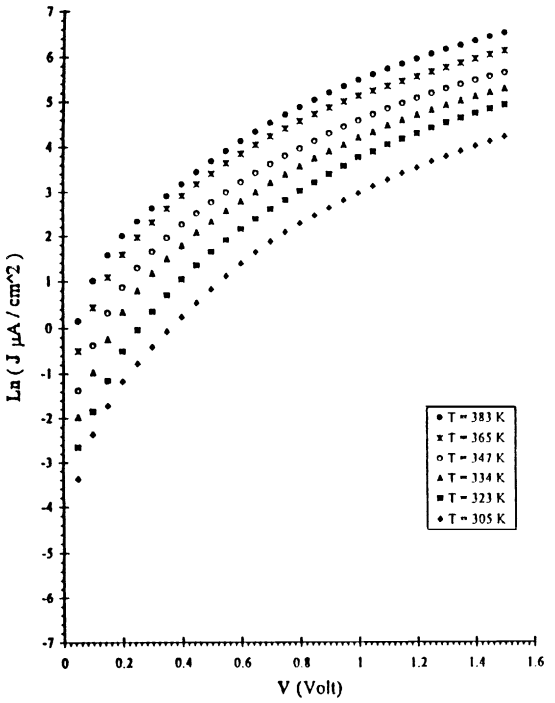

Fig. 9. Ln J versus forward applied bias Cell 3 at different temperatures.

magnitude indicate a reduction in the density of recombination state in the depletion layer of the cell.

In the second region ($0.3 < V < 0.8$) the plots are approximately parallel. In this region the I–V characteristics can be described by the equation

$$J = J_0 \exp(\alpha V), \tag{6}$$

indicating a tunneling controlled current.

Theoretically, an impurity concentration of 10^{19}–$10^{20}\,\mathrm{cm}^{-3}$ is necessary for direct band-to-band tunneling [16]. However, the density of acceptor states in the CdTe estimated from C–V measurements is about 10^{16}–$10^{17}\,\mathrm{cm}^{-3}$. This density is too low to allow single–step tunneling through the energy barrier. Hence, the tunneling might have occurred via the multiple-step process. Electrons tunnel from the conduction band of the n-material (CdS or $Cd_{0.9}Zn_{0.1}$ S) to the empty inter band states located in the p-CdTe and subsequently recombine through a staircase of closely spaced states in the depletion region. It can be concluded that, the current transport across the examined cells may be modeled as a combination of both multi-step tunneling and recombination at the interface. According to the theory presented by

Table 3
Values of α, III, ΔE_a, and ϕ_s for the three cells

Junction	α (V^{-1})	m	ΔE_a(eV)	ϕ_s (eV)
Cell 1	8.35	4.62	0.457	0.441
Cell 2	11.58	3.18	0.504	0.614
Cell 3	14.46	2.52	0.487	0.277

Table 4
Values of N_{IS}, W, N_A, and V_D for the three cells

Junction	N_{IS} (cm^{-2}/eV)	W (μ)	N_A (cm^{-3})	V_D (V)
Cell 1	3.33×10^{11}	0.14	1.1×10^{17}	2.2
Cell 2	2.80×10^{11}	0.18	4.3×10^{16}	1.3
Cell 3	2.08×10^{11}	0.31	1.0×10^{16}	0.97

Kindl and Touskova [17] assuming a sandwich structure consisting of a polycrystalline layer with several identical inter-granular (IG) barriers in series with a Schottky junction, the series resistance varies exponentially with temperature following the relation

$$R_s = R_{so}\exp(\varphi_s/KT), \quad (7)$$

where ϕ_s is the height of the IG barrier.

From $\ln R_s$ versus $1000/T$ plots shown in Fig. 10 for cell 3 as a representative example, the IG barrier height is found to have values as listed in Table 3 for the three cells. The presence of these barriers represents a serious obstacle to the charge carriers flowing through the bulk of the device.

3.2.1.2. Illuminated I–V characteristics. *I–V* characteristics of the cells are studied under illumination to get the photovoltaic parameters of these cells. The measurements were performed using a tungsten halogen lamp light source with an estimated light intensity 85 mW cm^{-2} for illumination. The illuminated *I–V* characteristics for the cells with a cell total area of 0.5 cm^2 are shown in Figs. 11–13. The observed open-circuit voltage (V_{oc}) values, determined from the intercept of the curve with the voltage axis ($J = 0$) for cells 1, 2 and 3 are 135, 180 and 295 mV, and the short-circuit current (J_{sc}) values, calculated from the intercept with the current axis ($V = 0$), for the cells 1, 2 and 3 are 0.2, 4.8 and 7.7 μA. The very low values of J_{sc} and V_{oc} may result from the high series resistance values, the low shunt resistance values, and the poor collection efficiency.

The poor collection efficiency is probably due to recombination losses in the bulk and in the interface region.

3.2.2. C–V characteristics

Capacitance dispersion measurements were used to determine the density of interface states. Fig. 14 shows the variation of the capacitance with frequency measured at zero bias for the three cells. It is clear that the capacitance decreases with increasing frequency. As the measuring frequency is decreased more deep levels at or near the

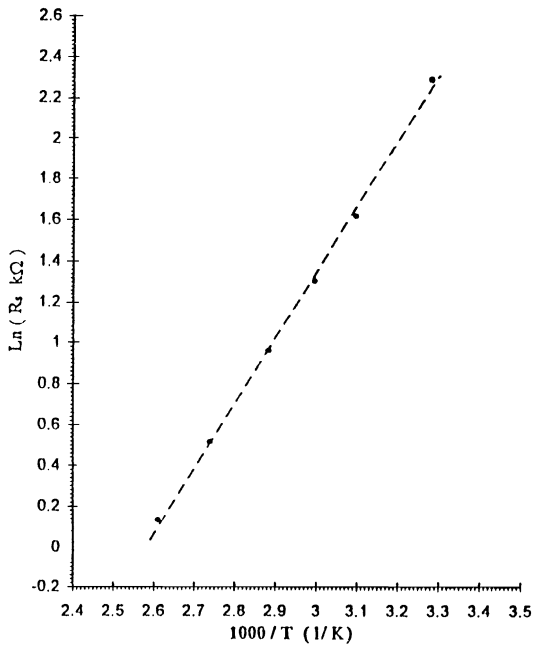

Fig. 10. $\ln R_s$ versus $1000/T$ for Cell 3.

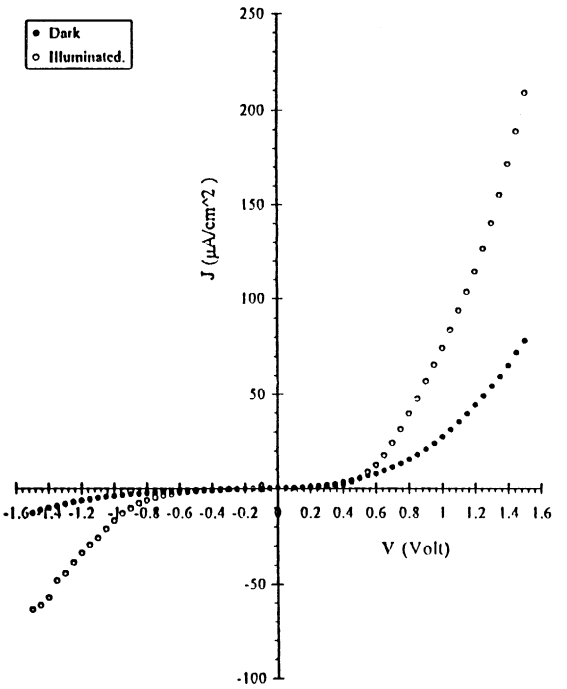

Fig. 11. Dark and illuminated *I–V* characteristics under 85 mW/cm^2 for Cell 1.

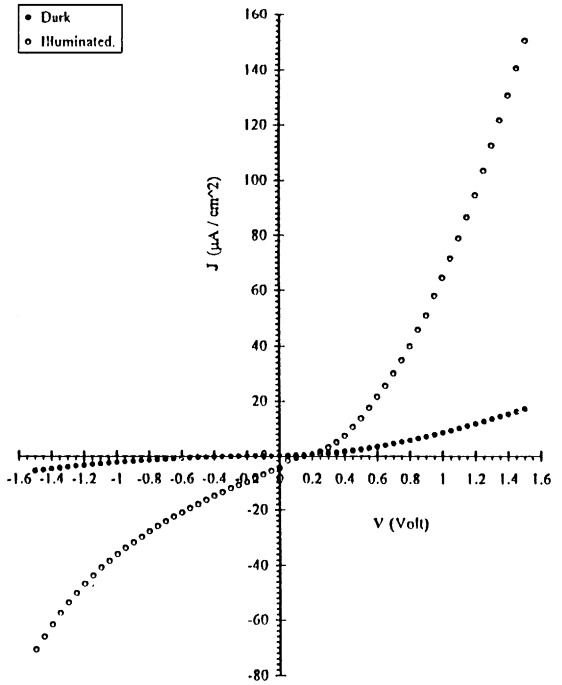

Fig. 12. Dark and illuminated I–V characteristics under 85 mW/cm^2 for Cell 2.

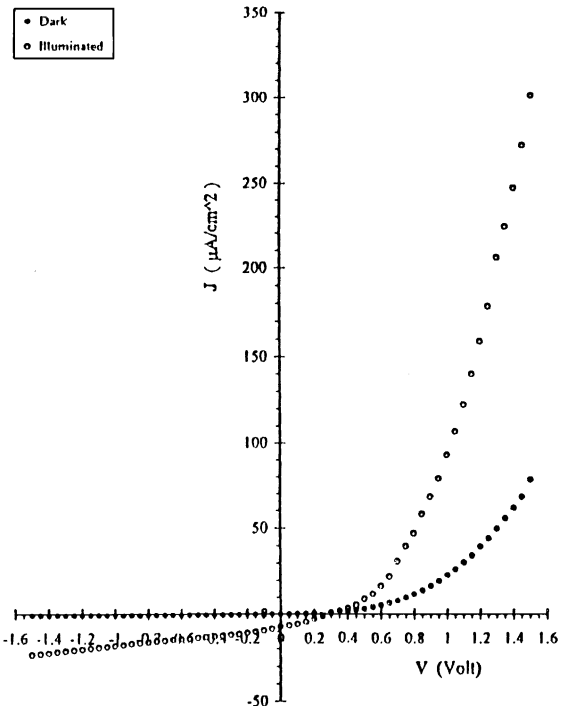

Fig. 13. Dark and illuminated I–V characteristics under 85 mW/cm^2 for Cell 4.

interface of $Cd_{0.9}Zn_{0.1}S$/CdTe (CdS/CdTe) are able to respond to the a.c. signal, hence generating a larger capacitance. The total number of states due to depletion and interface can be calculated from the capacitance measured at low frequency while the capacitance at higher frequency is associated with depletion only. A lower limit of the interface states (N_{IS}) can be calculated from the relation [18]

$$N_{IS} = (C_{LF} - C_{HF})/e, \tag{8}$$

where C_{LF} and C_{HF} are the capacitance at low ($f \sim 10$ Hz) and high ($f \sim 10^5$ Hz) frequency.

At a reverse bias (V) the capacitance of anisotype junction is primarily determined by the capacitance of the depletion region. The capacitance per unit area given by Shur [19]

$$C = [e\varepsilon_n N_D \varepsilon_P n/(\varepsilon_n N_d + \varepsilon_P N_A)]\,[1/2(V_D - V)^{1/2}]$$
$$= e\varepsilon N_{eff}/2(V_D - V)^{1/2}, \tag{9}$$

where ε is the medium permativity, N_{eff}, the effective carrier concentration, ε_N, ε_P, the permittivities and N_D, N_A ionized impurity density in the n-type and p-type materials, respectively.

By plotting C^{-2} versus V, the values of N_{eff} and V_D can be determined.

C–V characteristics of the three cells were measured at a frequency of 50 Hz in the dark and at room temperature. Fig. 15 shows the C^{-2} versus V plot for cell 3 as a representative example. The zero bias capacitance $C(0)$ was used to calculate the depletion layer width using the relation

$$W = \varepsilon/C(0), \tag{10}$$

where $\varepsilon \cong 10^{-10}$ F m^{-1} and is listed in Table 4. As obvious from the table, cell 3 has the widest depletion width compared to cell 1 and cell 2.

The carrier concentration N_A for the three cells was obtained from the slope of the C^{-2} versus V curve and listed in Table 4. The obtained values for V_D, 2.2 and 1.3 V for cell 1 and cell 2 are very

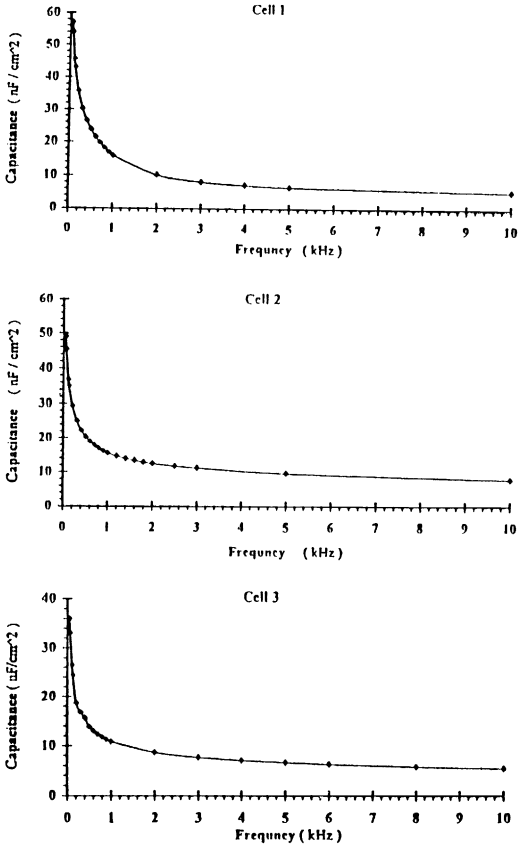

Fig. 14. Variation of the junction capacitance with the measuring frequency at zero bias.

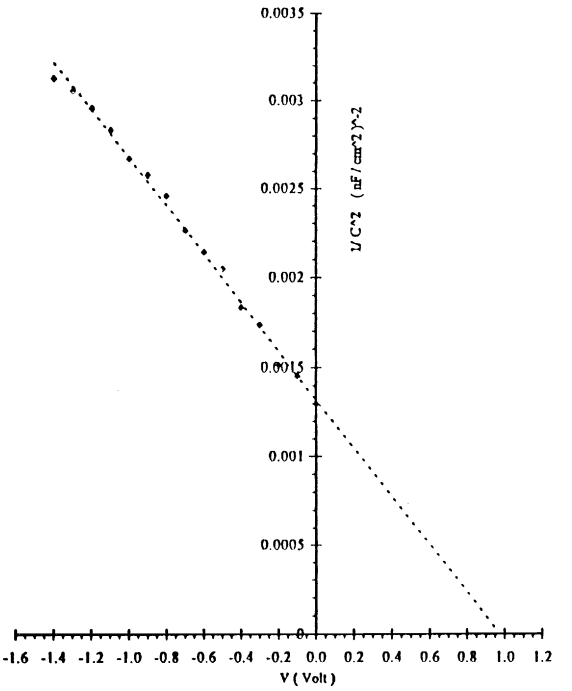

Fig. 15. *C–V* characteristics for Cell 3 at a measuring frequency of 50 Hz.

far from the values of V_D observed in the *I–V* characteristics. However, the value of $V_D = 0.97$ V from the *C–V* characteristics for cell 3 is comparable to that found from the *I–V* characteristics. The difference between the *C–V* results and the *I–V* results for V_D can be attributed to the high density of interface states as discussed above.

4. Conclusion

Thermally evaporated CdTe films are polycrystalline and belong to the cubic zinc blind structure. Recrystallization of CdTe films occurs during heat treatment with and without $CdCl_2$, but better film quality is obtained by heat treatment with $CdCl_2$. The heat treatment with and without $CdCl_2$ also increase the conductivity, and decrease both the activation energy and the optical energy gap which can be attributed to the improvement of the film crystallinity and the growth of grain size.Analysis of the dark *I–V* characteristics at different temperatures for (the three cells)

Cell 1: glass/Au grid/n-CdS/p-CdTe/Al

Cell 2: glass/Au grid/n-$Cd_{0.9}Zn_{0.1}S$/p-CdTe/Al

Cell 3: glass/Au grid/n-$Cd_{0.9}Zn_{0.1}S$/p-CdTe/Al, where $Cd_{0.9}Zn_{0.1}S$ is treated with $CdCl_2$ prior to CdTe deposition show that cell 3 has the best performence since it has the lowest series resistance, highest shunt resistance and the best rectification compared to the other cells.. This means that, $CdCl_2$ treatments improves the crystallinity and the surface morphology of the $Cd_{0.9}Zn_{0.1}S$ films leading to the improvement of the junction interface between $Cd_{0.9}Zn_{0.1}S$ and CdTe films. Also cell 3 shows the highest open-circuit voltage and short-circuit current compared to cell 1 and cell 2. However, the observed values of I_{sc} and V_{oc} are very low and may result from the

high series resistance, the low shunt resistance and the poor collection efficiency. The poor collection efficiency is probably due to recombination losses in the bulk and in the interface region. Capacitance dispersion measurements reveal a high density of interface states of cell 1 and cell 2 compared with cell 3. It is found that the depletion layer width increases when $Cd_{0.9}Zn_{0.1}S$ films are used as window layer instead of CdS and increases more upon treating with $CdCl_2$. Generally it can be concluded that $Cd_{0.9}Zn_{0.1}S$ films are good partner for CdTe to produce heterojunctions solar cells. Moreover, heat treatment with $CdCl_2$ can further improve the properties of these films, which is reflected as an improvement in the junction performance.

References

[1] Walf M. Proc IRE 1960;48:1246.

[2] Hasoon FS, Al-Jassim MM, Swartzlander A, Sheldon P, Al-Douri AAJ, Alnajjar AA. Proceedings of the 26th IEEE Photovoltaic Specialists Conference. California: IEEE, 1997.

[3] Anderson RL. Proceedings of International Conference on the Physics and Chemistry of Semiconductor Heterojunctions, vol. II, Budapest: Akademiai Kiado, 1971. p. 55.

[4] Anderson RL. Solid State Electron 1962;5:341.

[5] Birkmire RW, Phillips JE. Final Subcontract Report, National Renewable Energy Laboratory, Golden, CO, 1997.

[6] Al-Jassim MM, Hasoon FS, Jones KM, Keyes BM, Matson RJ, Moutinho RH. Proceedings of the 23rd IEEE Photovoltaic Specialists Conference. New York: IEEE, 1993. p. 459.

[7] Moutinho HR, Dhere RG, Ramanathan K, Sheldon P, Kazmerski LL. Proceedings of the 25th IEEE Photovoltaic Specialists Conference. New York: IEEE, 1996. p. 945.

[8] Waters DM, Niles D, Gessert TA, Albin D, Rose DH, Sheldon P. Surface Analysis of CdTe after Various Pre-Contact Treatments, Presented at the 2nd World Conference and Exhibition on Photovoltaic Solar Energy Conversion, Vienna, Austria, 1998.

[9] Morris GC, Tanner PG, Tottszer A. Proceedings of the 21st IEEE Photovoltaic Specialists Conference, Orlando. New York: IEEE, 1990. p. 485.

[10] Kroemer H. RCA Rev 1957;18:332;
Kroemer H. Proc IEEE 1963;51:1782.

[11] Morris GC, Venderven R. Sol Energy Mater Sol Cells 1992;26:217.

[12] Redwan MA, Laila SI, Aly EH, El-Shazely AA, Zayed HA, to be published.

[13] McCandless BE, Hegedus SS. Proceedings of the 22nd IEEE Photovoltaic Specialists Conference. New York: IEEE, 1991. p. 967.

[14] Das SK. Sol Energy Mater Sol Cells 1993;29:277.

[15] Bitar RA, Arafah DE. Sol Energy Mater Sol Cells 1998; 51:83.

[16] Chopra KL, Das SR, Thin Films Solar Cells, New York: Plenum, 1983. p. 325.

[17] Kindl D, Touskova J. Phys Stat Sol A 1988;106:297.

[18] Tavakolian H, Sites JR, Proc. 20th IEEE Photovoltaic Specialists Conference, Las Vegas, NV. New York: IEEE, 1988. p. 1608.

[19] Shur M, Physics of Semiconductor Devices, New York: Wiley, 1990. p. 170.